


## Multiscale design of large and irregular metamaterials

J. R. Capers<sup>1,\*</sup>, L. D. Stanfield<sup>1,†</sup>, J. R. Sambles<sup>1</sup>, S. J. Boyes<sup>2</sup>, A. W. Powell<sup>1</sup>, A. P. Hibbins<sup>1</sup> and S. A. R. Horsley<sup>1</sup>

<sup>1</sup>*Department of Physics and Astronomy, University of Exeter, Stocker Road, Exeter EX4 4QL, United Kingdom*

<sup>2</sup>*DSTL Porton Down, Salisbury, Wiltshire SP4 0JQ, United Kingdom*

 (Received 5 September 2023; revised 30 October 2023; accepted 5 December 2023; published 4 January 2024)

Next-generation microwave communications systems face several challenges, particularly from congested communications frequencies and complex propagation environments. We present, and experimentally test, a framework based on the coupled-dipole approximation for designing structures composed of a single simple emitter with a passive disordered scattering structure of rods that is optimized to provide a desired radiation pattern. Our numerical method provides an efficient way to model, and then design and test, otherwise inaccessibly large scattering systems.

DOI: [10.1103/PhysRevApplied.21.014005](https://doi.org/10.1103/PhysRevApplied.21.014005)

### I. INTRODUCTION

In recent years, metamaterials, man-made materials structured at the subwavelength scale, have attracted much interest due to their versatile wave-shaping capabilities. From invisibility cloaks [1,2] to perfect lenses [3], metamaterials offer novel ways to control and to shape the propagation of electromagnetic, acoustic, elastic [4], and water waves [5] as well as heat [6]. While early examples of metamaterials consist of periodically patterned metal [7] or dielectric [8], more recently, disorder has been exploited [9] to achieve a range of interesting wave effects such as antireflection coatings [10], energy storage [11], perfect absorption [12], analog computing [13], and imaging [14].

Disordered materials have also been employed to manipulate the radiation from subwavelength emitters [15–17]. In this context, the role of disorder is to provide many more design degrees of freedom to achieve the desired behavior. Engineering the radiation from small sources has many key applications for the next generation of microwave communications. Current networks face many challenges [18], particularly from congested communications frequencies and complex propagation environments. Rather than solving this complex propagation problem using a combination of a large number of antenna, one can instead try to move the functional complexity into

a metamaterial layer that can reshape the radiation from a given single source in a desired way and that may be easily fabricated and modified to change functionality. A key question is, therefore, how to design such a metamaterial layer to structure, in a specified way, the radiation pattern of an emitter.

Several methods for designing passive scattering structures to manipulate the radiation from an emitter have been developed over the past decade. Utilizing elegantly simple phase-based arguments, structures have been designed [19] and experimentally realized [20] that enhance the radiation efficiency of an emitter by factors in the thousands. Methods based on perturbation theory [21,22] and shape optimization [23] have been utilized in quantum electrodynamics to control energy transfer and enhance coherence. The adjoint method [24] has enabled efficient the topology optimization of photonic components (see, e.g., Ref. [25]) and deep learning [26,27] has been utilized to solve both forward and inverse problems. While powerful, the adjoint method can produce graded structures that are difficult to manufacture and physical insight can be difficult to extract from deep-learning techniques. Genetic algorithms have also been employed [15–17] to distribute scattering elements to produce antenna with specific radiation properties. In the context of antenna engineering, disordered phased arrays have been designed using genetic algorithms [28,29] and sparse optimization [30–32]. Parasitic antenna arrays have been well known for many years [33,34]; however, these typically involve a small number of parasitic elements due to the numerical demands of modeling and optimizing such systems.

In this work, we design and experimentally realize disordered arrangements of scatterers (metal rods) around a single emitter to engineer the far-field radiation pattern of the

\*j.capers@exeter.ac.uk

†lds211@exeter.ac.uk

*Published by the American Physical Society under the terms of the [Creative Commons Attribution 4.0 International](https://creativecommons.org/licenses/by/4.0/) license. Further distribution of this work must maintain attribution to the author(s) and the published article's title, journal citation, and DOI.*

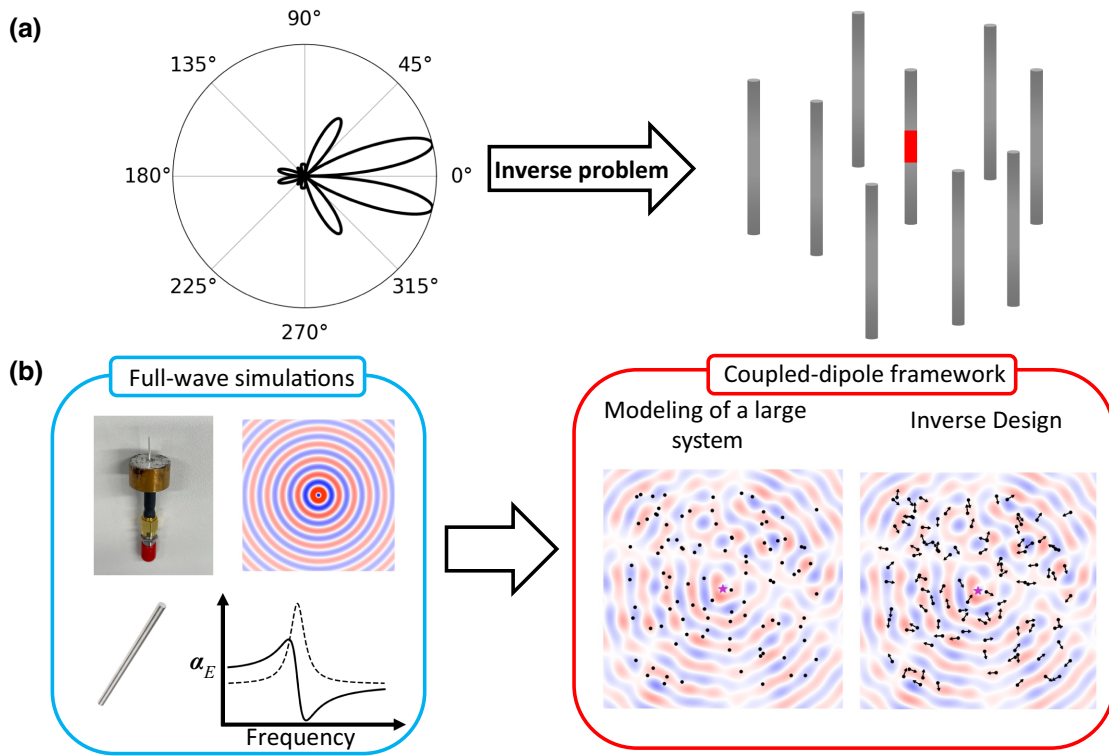


FIG. 1. (a) The particular physical problem with which we illustrate our method is how to distribute scatterers around an emitter to engineer the far-field radiation pattern in a particular way. (b) Our proposed method is to combine full-wave simulations of the building blocks of a large scattering material with the coupled-dipole framework to enable both the modeling and design of irregular metamaterials, for a range of applications.

emitter in a particular plane. This is shown schematically in Fig. 1(a). Our proposed design approach, illustrated in Figure 1(b), exploits the multiscale nature of the problem. The building blocks of the system, the emitter and the rods, can be modeled individually using full-wave simulations. The resulting properties can be imported into semianalytical coupled-dipole code, to enable the modeling and inverse design of a large irregular metamaterial. Crucially, this technique enables the modeling and design of systems that are too large for full-wave simulations and is applicable to a wide range of problems from radiation pattern shaping to wave-front manipulation. While we focus on the particular problem of rods reshaping the radiation from an emitter, our approach includes all of the physics of three-dimensional vector electromagnetism and is flexible enough to be applicable to wave-front shaping [10], smart radio environments [35], and random lasing or absorption [12,36], as well as to other wave regimes such as acoustics and elasticity.

## II. THEORY, MODELING, AND INVERSE DESIGN

Before attempting to design the structures, we will develop an efficient way to model them so that all of the fields of the system can be extracted and analyzed efficiently. Modeling a system comprised of a large number

of scattering elements around an emitter is generally very challenging. In finite-element or finite-difference full-wave solvers, the length-scale separation between the subwavelength scattering elements and the tens of wavelengths that make up the whole structure can result in intractably large simulations. To avoid this, we utilize the coupled-dipole approximation [37,38]. Assuming that each of the passive scatterers can be described as a point dipole located at position  $\mathbf{r}_n$ , scattering from these introduces source terms in Maxwell’s equations related to the polarization and magnetization densities,

$$\mathbf{P} = \sum_n \alpha_E \mathbf{E}(\mathbf{r}_n) \delta(\mathbf{r} - \mathbf{r}_n), \quad (1)$$

$$\mathbf{M} = \sum_n \alpha_H \mathbf{H}(\mathbf{r}_n) \delta(\mathbf{r} - \mathbf{r}_n), \quad (2)$$

where  $\alpha_E$  is the electric polarizability of the scatterer and  $\alpha_H$  is the magnetic polarizability. These tensors relate the applied electric and magnetic fields,  $\mathbf{E}$  and  $\mathbf{H}$ , to the polarization and magnetization densities,  $\mathbf{P}$  and  $\mathbf{M}$ . More complicated scattering elements can be described in this framework if one includes additional multipolar terms in the electric and magnetic polarizabilities [39,40]. In this

work, we restrict ourselves to the case where all of the scatterers can be described as dipoles. With these source terms, the solution to Maxwell's equations can be written as

$$\phi(\mathbf{r}) = \phi_{\text{inc}}(\mathbf{r}) + \sum_{n=0}^N \mathbb{G}(\mathbf{r}, \mathbf{r}_n) \phi(\mathbf{r}_n), \quad (3)$$

where we have adopted the compact notation of Ref. [41], that

$$\phi(\mathbf{r}) = \begin{pmatrix} \mathbf{E}(\mathbf{r}) \\ \eta_0 \mathbf{H}(\mathbf{r}) \end{pmatrix}, \quad (4)$$

$$\mathbb{G}(\mathbf{r}, \mathbf{r}') = \begin{pmatrix} \xi^2 \mathbf{G}(\mathbf{r}, \mathbf{r}') \boldsymbol{\alpha}_E & i\xi \mathbf{G}_{EH}(\mathbf{r}, \mathbf{r}') \boldsymbol{\alpha}_H \\ -i\xi \mathbf{G}_{EH}(\mathbf{r}, \mathbf{r}') \boldsymbol{\alpha}_E & \xi^2 \mathbf{G}(\mathbf{r}, \mathbf{r}') \boldsymbol{\alpha}_H \end{pmatrix}, \quad (5)$$

where

$$\mathbf{G}(\mathbf{r}, \mathbf{r}') = \left[ \mathbf{1} + \frac{1}{\xi^2} \nabla \otimes \nabla \right] \frac{e^{i\xi|\mathbf{r}-\mathbf{r}'|}}{4\pi|\mathbf{r}-\mathbf{r}'|} \quad (6)$$

is the Dyadic Green's function [42],  $\xi = ka$  is a dimensionless wave number with  $a$  being a characteristic length scale of the problem,  $\eta_0$  is the impedance of free space, and  $\mathbf{G}_{EH} = \nabla \times \mathbf{G}(\mathbf{r}, \mathbf{r}')$ . It should be noted that the fields applied to each scatterer  $\phi(\mathbf{r}_n)$  must be calculated by imposing self-consistency [41,43], resulting in a matrix of size  $6N \times 6N$  that must be inverted. This is the main computational burden of the coupled-dipole method but it ensures that all mutual coupling effects are fully accounted for.

Inverse design of the system is then facilitated according to the method presented by Capers *et al.* [43]. Starting from an initial distribution of scattering elements, the aim is to derive an analytical expression to find how to iteratively move the scatterers in order to increase a chosen figure of merit. To do this, we ask how moving a scatterer by a small amount changes the fields of the system. Perturbatively expanding the position of the scatterers,

$$\delta(\mathbf{r} - \mathbf{r}_n - \delta\mathbf{r}_n) = \delta(\mathbf{r} - \mathbf{r}_n) - (\delta\mathbf{r}_n \cdot \nabla) \delta(\mathbf{r} - \mathbf{r}_n) + \dots, \quad (7)$$

one can find [41,43] that the change produced in the field is

$$\delta\phi(\mathbf{r}) = \mathbb{G}(\mathbf{r}, \mathbf{r}_n) \nabla \phi(\mathbf{r}_n) \cdot \delta\mathbf{r}_n. \quad (8)$$

As our aim is to shape the far-field radiation pattern of the system, we define as our figure of merit the overlap integral in the far field in the plane of the scatterers,

$$\mathcal{F} = \frac{1}{\mathcal{N}} \int_0^{2\pi} d\phi |\mathbf{E}(\phi)| |\mathbf{E}_{\text{target}}(\phi)|, \quad (9)$$

where  $\mathcal{N}$  is a normalization factor that depends upon both  $\mathbf{E}$  and  $\mathbf{E}_{\text{target}}$ . This figure of merit ranges from 0 to 1, when

the radiation pattern is exactly the same as the target radiation pattern. This can be expanded under small changes of the field [41] to find an analytical expression for the gradient of the figure of merit with respect to the positions of the scatterers. The expression is given in the Supplemental Material [44]. With this gradient found, elementary gradient-descent optimization,

$$\mathbf{r}_n^{i+1} = \mathbf{r}_n^i + \gamma \nabla_{\mathbf{r}_n} \mathcal{F} \quad (10)$$

where  $\gamma$  is the step size, can be used to iteratively update the positions of the scatterers to increase the figure of merit.

In order to use this framework to describe our experimental system, certain properties of the scatterers and the emitter must be extracted numerically. For scatterers, we use metal rods of length 15 mm and diameter 3 mm. These parameters have been chosen so that the dipole resonance of the rods will be at approximately 10 GHz, although any subwavelength resonator could be utilized. The polarizability tensors,  $\boldsymbol{\alpha}_E$  and  $\boldsymbol{\alpha}_H$ , can be found using full-wave simulations following the prescription of Yazdi *et al.* [45,46]. Exciting the rod with plane waves from different directions, the induced charges and currents can be integrated to find the electric and magnetic dipole moments, which can be related to columns of the polarizability tensor. A schematic of the finite-element model is shown in Fig. 2(a), with the resulting  $z$  component of the polarizability as a function of frequency shown in Fig. 2(b). All other components of  $\boldsymbol{\alpha}_E$  and  $\boldsymbol{\alpha}_H$  are negligible. Electing to work at 7 GHz, the dipole resonance of the rods, the polarizability is

$$\boldsymbol{\alpha}_E = \begin{pmatrix} 0 & 0 & 0 \\ 0 & 0 & 0 \\ 0 & 0 & 1 \end{pmatrix} (6.91 + i14.17). \quad (11)$$

For the scatterers to be lossy, the polarizability tensor must obey the inequality  $\text{Im}[\boldsymbol{\alpha}_E] \geq \mathbf{1}k^3/(6\pi\epsilon)$  [47], where  $\epsilon$  is the permittivity of the background medium containing the scatterer. The other key component of the coupled-dipole approximation in Eq. (3) that we require is the field due to the source emitter. Our choice of emitter, a sleeve antenna, is shown in Fig. 2(c). The fields of the emitter on its own are calculated using COMSOL MULTIPHYSICS [48], shown in Fig. 2(d), then exported and interpolated to provide a function for the source fields that is fast to evaluate. As the scatterers have only a single nonzero component of their polarizability tensors, only the  $z$  component of the electric field is relevant. Correctly representing the source field is key to using this method to correctly design wave-shaping devices. As such, a complete numerical and experimental characterization of the emitter is included in Supplemental Material [44]. While we have made particular choices for the emitter and the scatterers, our design methodology is easily

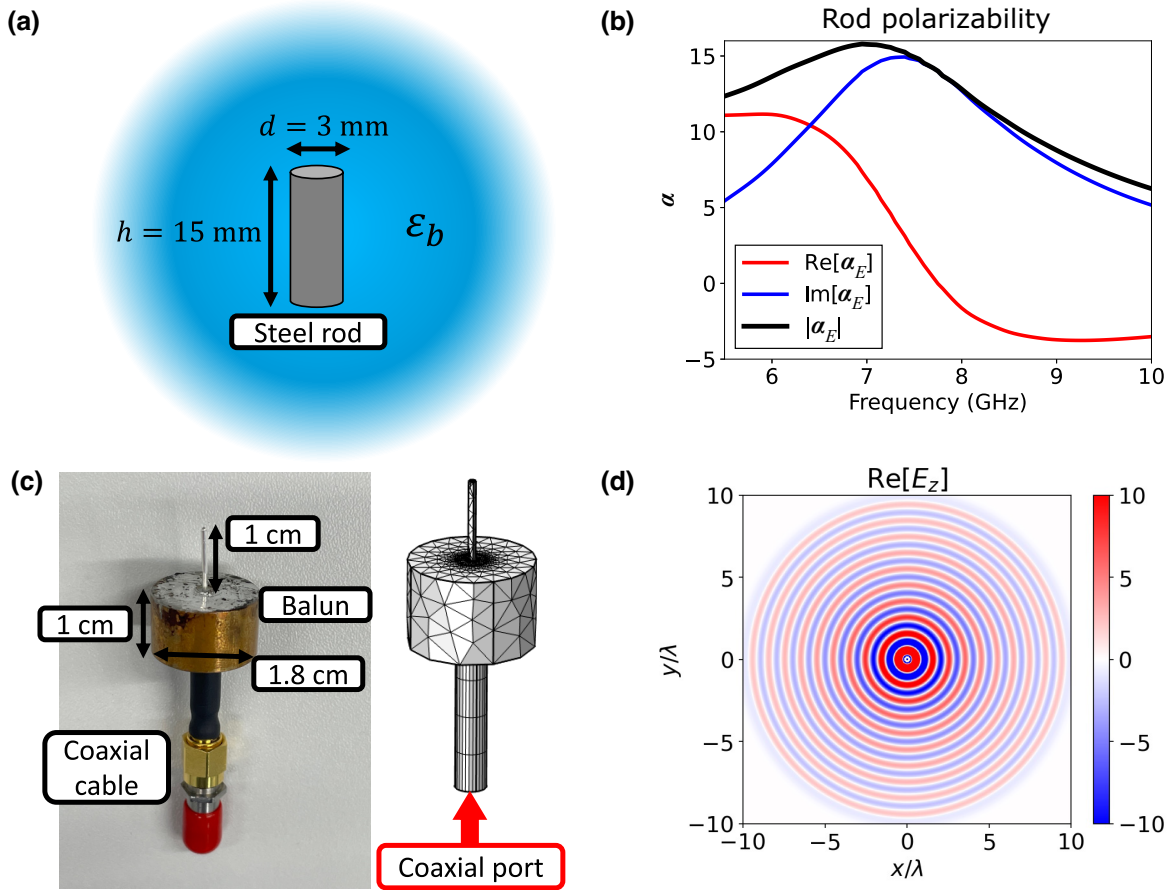


FIG. 2. The finite-element modeling of the scatterers and emitter. (a) A schematic of the finite-element model used to calculate the polarizability of the rods. (b) The resulting polarizability. (c) A photograph and finite-element representation of the source. (d) The calculated radiation field.

applicable to other systems. For example, this framework could be applied to the higher frequencies required for next-generation communication systems. In this context, the scattering elements could be patches and the source field due to, i.e., a Gaussian beam antenna. With such a setup, millimeter wave metasurfaces have been experimentally realized [49], operating at 83 GHz. Since the properties of the scatterers and source field are extracted numerically, the wavelength of operation does not affect the applicability of our techniques.

With the polarizability of the scatterers and the emitter characterized, the coupled-dipole framework can be used to both model and design a system with a specific radiation pattern. An investigation of how well the coupled-dipole framework describes the system is included in the Supplemental Material [44]. The key benefit of our approach is that the numerical complexity of the model depends upon the number of scatterers,  $N$ , involving the inversion of a matrix of the size  $6N \times 6N$ . Conversely, most full-wave solvers must solve linear systems that depend upon the size of the computational domain. For the structures that we consider here, this could be a volume of

approximately  $1000\lambda^3$ , resulting in hundreds of thousands of mesh elements. Indeed, describing large systems of aperiodic subwavelength scatterers in this way currently requires specialist computers, while the coupled-dipole framework can be run on a modest laptop. Our simulations and inverse design have been carried out using in-house coupled-dipole code written in PYTHON. Running on a Windows PC with a Intel® Xeon® CPU E5-2630 v2 @ 2.60 GHz processor, optimization of a 100-scatterer systems takes around 15 h and requires approximately 500 MB of RAM. For comparison, on the same machine, a single field calculation for the same system in COMSOL MULTIPHYSICS takes around 1 h and requires 120 GB of RAM. Consequently, our approach enables the design of otherwise inaccessible structures.

### III. EXPERIMENTAL RESULTS

Utilizing the modeling and design framework based on the coupled-dipole approximation, we have designed several devices that illustrate both the capabilities and limitations of our approach. Keeping the scatterers in the



plane of the emitter, for simplicity, the design approach outlined in Sec. II has been employed to design structures of 100 metal rods, driven by a central emitter, that have specified radiation patterns. The number of scatterers and their initial configuration are chosen arbitrarily. While the results of gradient-based optimizations are dependent upon the starting position in solution space, how to find a reasonable starting configuration remains an open challenge. Progress on this has been made in the context of graded dielectric systems [50]. Alternatively, one could develop an additive framework [21], whereby scatterers are added to an initially “empty” system or utilize a global optimization technique such as a genetic algorithm. Despite these challenges, we shall demonstrate that even an arbitrary choice of starting configuration produces effective devices that may be satisfactory depending upon the particular context of the problem. Once designed and constructed, the structures have been experimentally characterized using an Anritsu MS46122B vector network analyzer (VNA) and

a rotational table controlled by a Thorlabs APT precision motion controller. To determine the far-field radiation pattern, the structure has undergone a full 360° rotation in 1° increments about the z axis, parallel to the axis of the source and the rod scatterers, in an anechoic chamber, with the response measured by a Narda standard gain horn (Model 642) for the frequency range from 4.0 GHz to 10.0 GHz, in 0.05-GHz increments. A photograph of the experimental setup is given in the Supplemental Material [44].

The first example that we present is shown in Fig. 3. Our target radiation pattern is a unidirectional beam at 0° with a beam width of 10°. We decide to undertake our optimization based on an initial square array of 100 rods with periodicity  $0.75\lambda \sim 3$  cm, shown in Fig. 3(a). The scatterers are redistributed by optimizing the overlap integral in Eq. (9). A low-index disk of Evonik Industries Roacelle IG foam, of permittivity 1.05 and loss tangent 0.0017 at 10 GHz, is used to support the rods, which sit snugly within

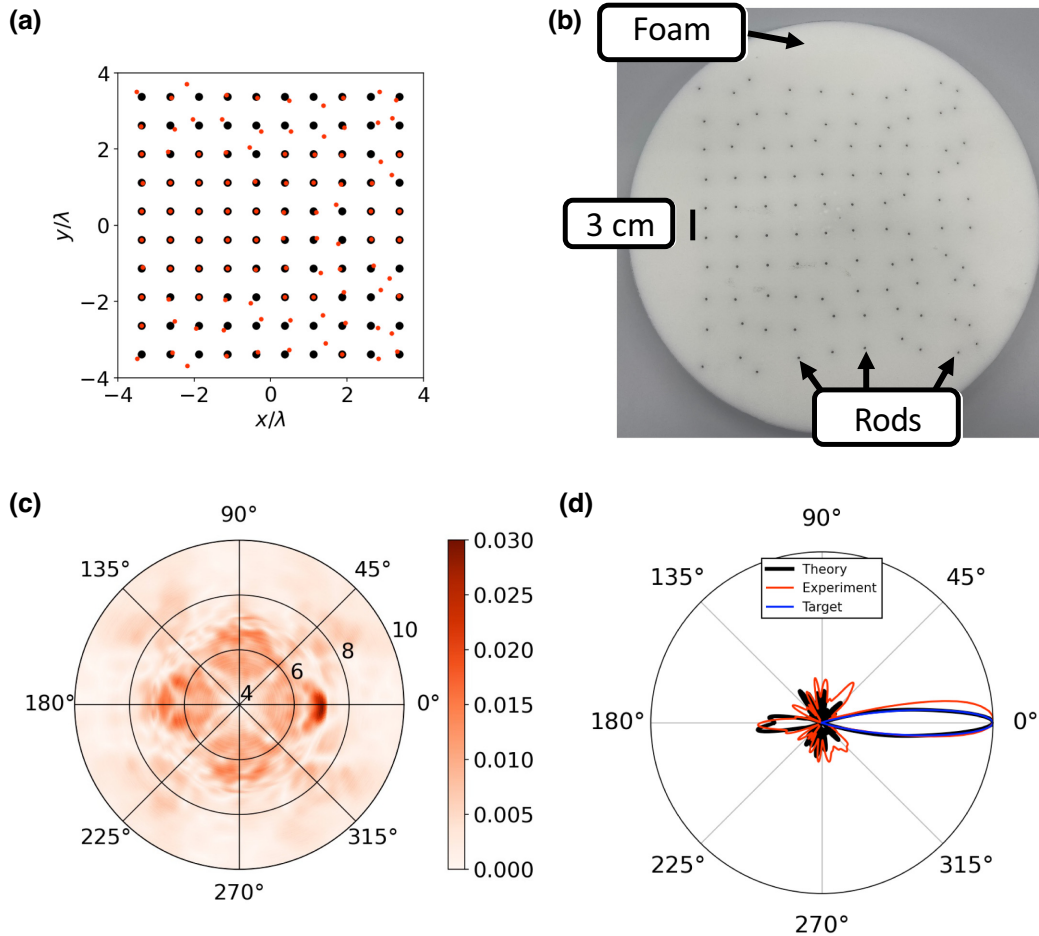


FIG. 3. Designing a 100-scatterer structure giving a beam in a single direction of width 10°. (a) The initial and final positions of the rods, with the emitter located at the origin: black, initial; red, optimized. (b) The experimental sample. (c) The radiation-pattern ( $|E|$ ) data, where the radial axis is the frequency in gigahertz. (d) Taking a cut of these data at 7 GHz, the theory, experimental and desired radiation patterns are presented.

the disk of thickness equal to the height of the rods. The constructed device is shown in Fig. 3(b), with the measured radiation pattern shown in Fig. 3(c). A clear peak can be seen at the design frequency of 7 GHz. Plotting the radiation pattern on a linear scale in Fig. 3(b), a beam at the correct location with a width close to the desired width is observed. It should be noted that over the course of the optimization, the rods move a distance similar to the original lattice spacing. To prevent rods touching or becoming coincident, updates that take the rods closer than  $2r$ , where  $r$  is the radius of the rods, are blocked. While we have chosen to work with 100-scatterer systems, we consider whether other numbers of scatterers give a better result. The details of this analysis are given in the Supplemental Material [44]. We find that increasing the number of scatterers increases the final figure of merit; however, the run time scales as  $N^{2.6}$ . There is therefore a trade-off between device performance and design time. Additional complexity is presented, however, by the fact that scatterers cannot cross each other during the optimization procedure. This restriction means that we exclude designs where the dipoles are very closely spaced, due to the potential breakdown of the dipole approximation.

Nevertheless, this is not a fundamental restriction and the method could be modified to include a more accurate modeling of the scatterer-scatterer interaction. As a result, the higher performance achieved by adding more scatterers does not preclude the existence of smaller designs that perform equally as well, if not better. However, the search space is very large and the system is strongly interacting, so there are few design strategies that could find such minima. Even genetic algorithms are likely to find local minima for such a problem [15].

In our next example, we design a device that has two beams of defined width at particular angles in the plane of the array. We choose to place one beam at  $350^\circ$  and another at  $260^\circ$ , both of width  $15^\circ$ . The corresponding device is shown in Fig. 4. The locations of the scatterers before and after the optimization are shown in Fig. 4(a), while the fabricated structure is shown in Fig. 4(b). In the measured radiation pattern, shown in Figs. 4(c) and 4(d), one can observe the expected features. Lobes at  $350^\circ$  and  $260^\circ$  are present and have the correct width.

Finally, to demonstrate the flexibility of our method, we design a device that has beams of different widths in three different directions, also with different relative

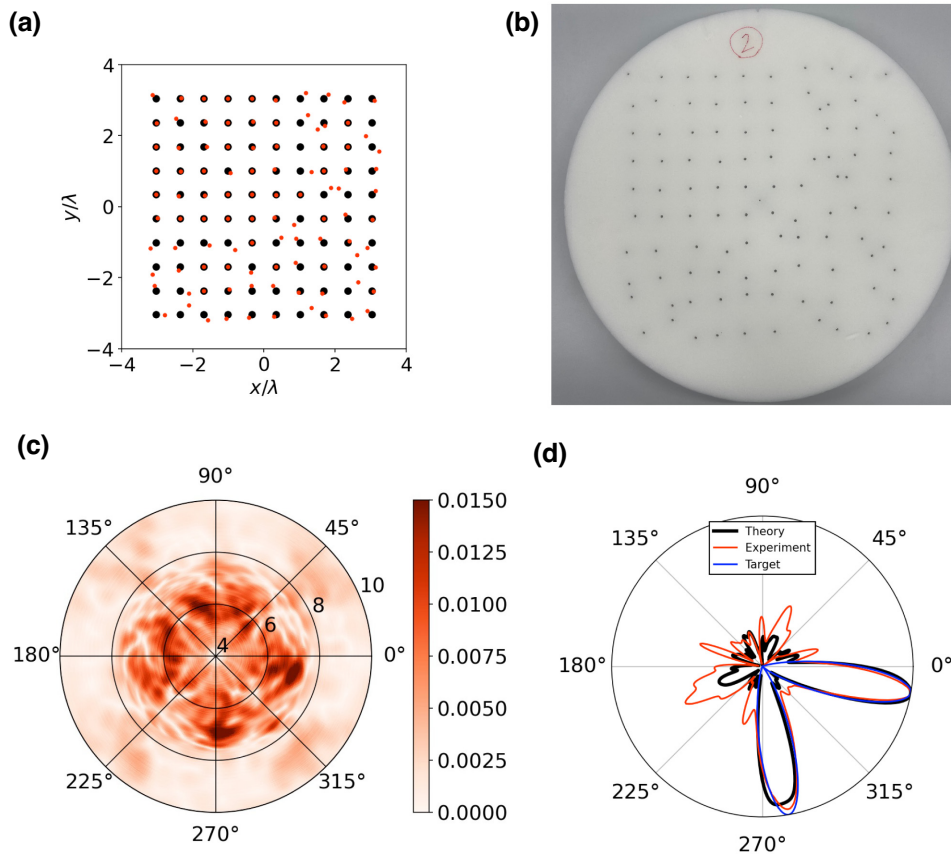


FIG. 4. Designing a device that beams into  $350^\circ$  and  $260^\circ$ , with beam widths of  $15^\circ$ . (a) The initial and final rod locations: black, initial; red, optimized. (b) The fabricated sample. (c) The measured radiation pattern ( $|E|$ ), with the radial axis being the frequency in gigahertz. (d) A cut of the far field taken at 7 GHz, compared with the theoretical predictions.

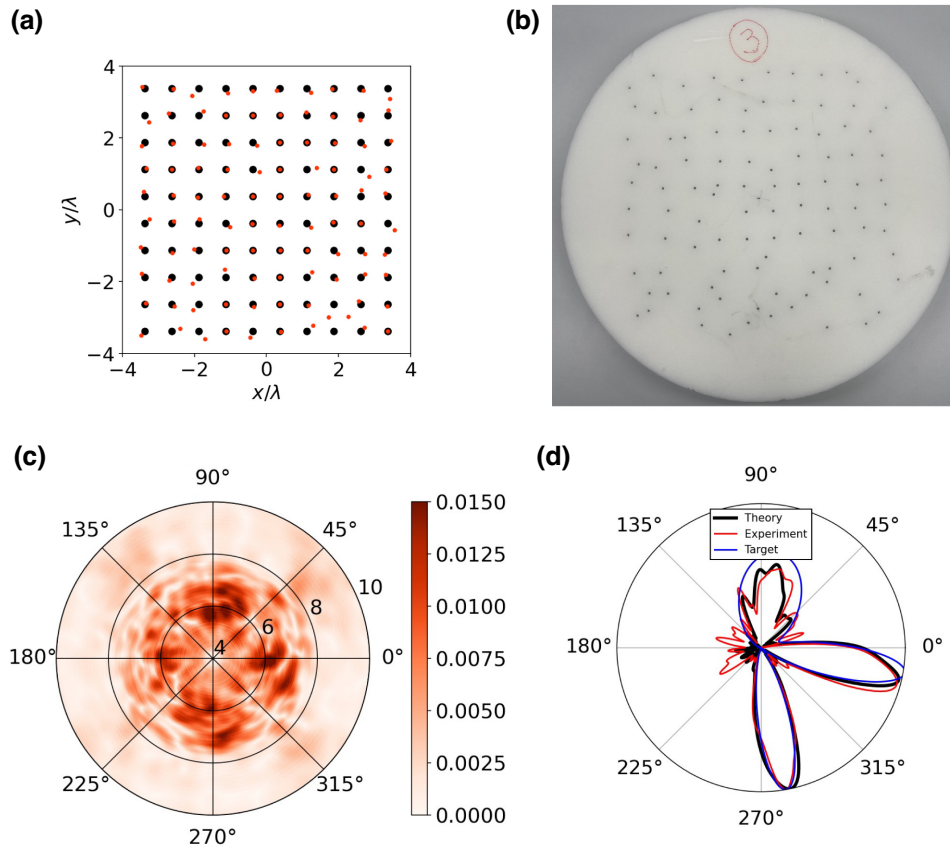


FIG. 5. Designing a device with two beams of maximum amplitude and width  $15^\circ$  at  $260^\circ$  and  $350^\circ$ , plus a beam of half amplitude at  $80^\circ$  with width  $45^\circ$ . (a) The initial and final rod locations: black, initial; red, optimized. (b) The experimental sample. (c) The measured radiation pattern ( $|E|$ ), where the radial axis is the frequency in gigahertz. (d) A comparison between experiment and theory.

far-field amplitudes. As shown in Fig. 5, we have aimed to design a device that has two beams of width  $15^\circ$  at  $350^\circ$  and  $260^\circ$  at maximum amplitude and a beam at  $80^\circ$  of width  $45^\circ$  at half-maximum amplitude. The locations of the rods before and after the optimization are shown in Fig. 5(a), while the device is shown in Fig. 5(b). The measured radiation pattern, illustrated in Fig. 5(c), shows the maximum-amplitude beams at  $200^\circ$  and  $250^\circ$ , with the half-amplitude beam at around  $100^\circ$ . Taking a slice at 7 GHz, as shown in Fig. 5(d), we see that the two full-amplitude beams occur at the correct positions and have the correct widths. The half-amplitude beam is at the correct position with an approximately correct width and amplitude.

While we have presented one-, two-, and three-beam examples, one could, in principle, define any radiation pattern as the target and seek to distribute scatterers to increase this figure of merit. Numerically, the limitation to this will be one's ability to find a good initial distribution of scatterers [50]. Physically, one is limited by (i) how strongly the elements of the metasurface scatter and (ii) the aperture of the device. Generally, stronger scattering elements give more control over the field and a larger

aperture allows for sharper features in the far-field to be captured.

While we aim to shape the radiation in the plane of the emitters, for completeness, the full far-field radiation pattern sphere for each device is shown in Fig. 6. The white dashed line indicates the plane in which the radiation pattern has been structured. One can observe that for both the one- and two-beam structures, shown in Figs. 6(a) and 6(b) respectively, most of the radiation is localized to the plane of the emitters. However, the radiation pattern of the three-lobe structure, illustrated in Fig. 6(c), shows significant out-of-plane radiation. To avoid this unwanted radiation, one could define the figure of merit as an overlap integral over the full far field.

We also consider the bandwidth of our devices. This is calculated by evaluating the overlap integral [see Eq. (9)] between the target distribution and the measured radiation pattern as a function of the frequency and is shown in Fig. 7. All of the devices are rather narrow band, or frequency selective, due to the high-order multiple-scattering effects that lead to the desired behavior. Each device performs the best at around 7 GHz, as expected. Measurements of the return loss,  $|S_{11}|$ , of our devices are

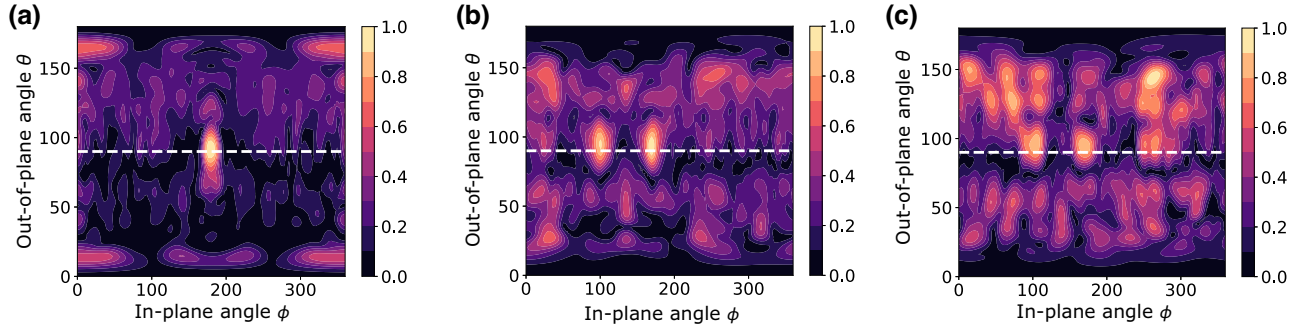


FIG. 6. The full far-field spheres of the devices shown in (a) Fig. 3 (one-beam design), (b) Figs. 4 (two-beam design), and (c) Fig. 5 (three-beam design). The white dashed line indicates the plane in which the radiation pattern has been optimized.

given in Supplemental Material [44]. For the one- and two-beam devices,  $|S_{11}|$  is comparable to that of the emitter in free space. The three-beam device, however, exhibits an increase in return loss from  $|S_{11}| = 0.1$  to  $|S_{11}| = 0.3$ .

While these experimental results show clear proof of concept, the experimental and theoretical results do not align perfectly. Many steps in constructing both the experiments and the semianalytical design framework introduce non-negligible sources of error. Approximating the rods as dipoles is well justified, as their quadrupole moment has been calculated to be approximately 5 orders of magnitude lower than the dipole moment. However, treating them as point dipoles, rather than distributed currents, introduces deviations in the radiation pattern due to near-field effects. Provided that the rods are separated by a distance larger than 5 times the radius, as is the case in all of the designs we have presented, this induces a small but constant error in the far-field radiation pattern. Next, the effect of small errors in the measurement of the permittivity of the foam has been considered. An over- or under-estimation of the permittivity by approximately 1% has been found to have little effect; however, once the error reached approximately 5%, large differences in both the main and back lobes have

been observed. Importantly, the back lobes become larger relative to the main lobes, as we observe in the experimental data. Furthermore, errors in the estimation of the polarizability of the rods can also introduce additional back lobes. A slightly different  $\alpha_E$  could be caused by small inconsistencies in the lengths of the rods. We find that a 5% difference in the length of the rods can change the polarizability enough to introduce the back lobes observed in the experimental data. One way to remedy this could be to infer  $\alpha_E$  from experimentally measured radiation patterns. The full data generated for these investigations are given in the Supplemental Material [44].

#### IV. ANALYSIS OF THE DESIGNS

One can leverage the analytical framework of the coupled-dipole approximation to provide physical insight into the structures that we have designed. When setting up the problem in Sec. II, it was pointed out that using the coupled-dipole framework to describe all of the interactions in the system involves assembling and inverting a matrix [51]. This matrix describes all of the interactions in the system and can be used to characterize

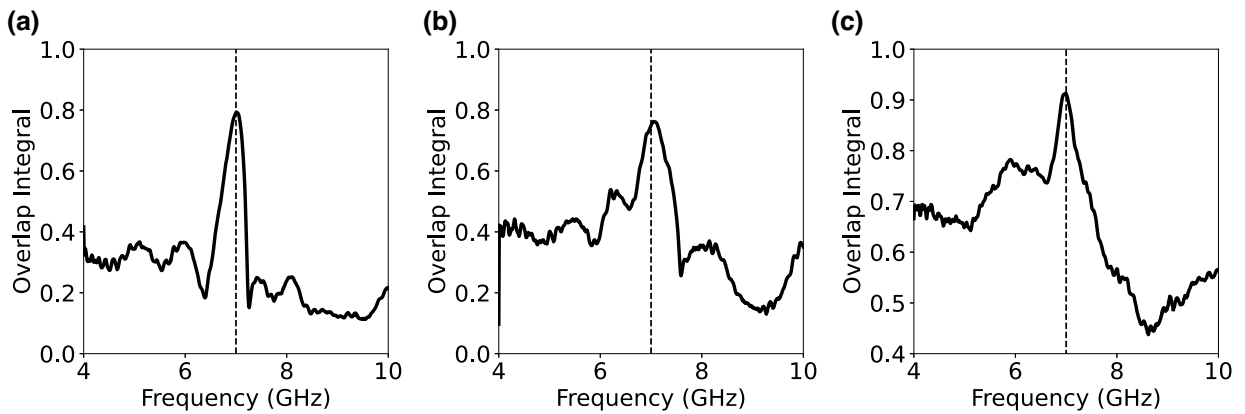


FIG. 7. The frequency response of our devices, calculated by evaluating the overlap integral given in Eq. (9), with the measured radiation patterns: (a) one-beam device; (b) two-beam device; (c) three-beam device. The dashed line indicates 7 GHz, the design frequency.



multiple-scattering effects in complex systems [43]. When setting up the multiple-scattering problem, one must construct the following self-consistency condition:

$$\mathbf{A}_{nm}\boldsymbol{\phi}_m = \boldsymbol{\phi}_{\text{inc},n}, \quad (12)$$

where  $\mathbf{A}_{nm} = \mathbf{1}\delta_{nm} - \mathbb{G}(\mathbf{r}_n, \mathbf{r}_m)$ ,  $\boldsymbol{\phi}_m = \boldsymbol{\phi}(\mathbf{r}_m)$ , and  $\boldsymbol{\phi}_{\text{inc},n} = \boldsymbol{\phi}_{\text{inc}}(\mathbf{r}_n)$ , in order to correctly describe all of the interactions within the system. The matrix  $\mathbf{A}$  can be inverted to rewrite this as

$$\boldsymbol{\phi} = \mathbf{R}\boldsymbol{\phi}_{\text{inc}}, \quad (13)$$

where we define  $\mathbf{R} = \mathbf{A}^{-1}$  as the interaction matrix and we have dropped the indices. This matrix describes the effect of the system on the incident field  $\boldsymbol{\phi}_{\text{inc}}$ . The eigenvectors of this matrix describe field configurations corresponding to certain collective responses of the system. How strong these collective responses are is given by the associated eigenvalue  $\lambda$ , with large  $|\lambda|$  corresponding to a large collective response. The ability to provide physical insight into the interactions of the system is a key benefit of our framework. Similar antenna-design methodologies either seek to minimize the coupling between elements [28,31,32] or employ full-wave simulations to take them into account [29,30]. While the latter approach includes multiple-scattering effects, it offers little insight into which collective responses are important. In this section, we shall explore the interactions in the systems we have designed, seeking to elucidate the features of our devices that are important for performance.

We will seek to decompose the fields at the scatterers into the eigenmodes of the interaction matrix, to explore which modes contribute most to the response of the system. As the matrix  $\mathbf{R}$  has no obvious symmetries, its eigenvectors do not form an orthogonal basis. However, we can work in terms of the right,  $\mathbf{v}$ , and left,  $\mathbf{w}$ , eigenvectors, which satisfy

$$\mathbf{R}\mathbf{v} = \lambda\mathbf{v}, \quad \mathbf{w}\mathbf{R} = \lambda\mathbf{w}, \quad \mathbf{w}_n^\dagger \cdot \mathbf{v}_m = \delta_{nm}. \quad (14)$$

Here,  $\mathbf{w}_n^\dagger$  represents the conjugate transpose of the  $n$ th (right) eigenvector. One can then decompose the field at the scatterers into this basis:

$$\boldsymbol{\phi} = \sum_{n=0}^N c_n \mathbf{v}_n, \quad (15)$$

where  $N$  is the total number of eigenmodes and the expansion coefficients  $c_n$  are found according to

$$c_n = \mathbf{w}_n^\dagger \cdot \boldsymbol{\phi}. \quad (16)$$

Now, to analyze the behavior of our devices, we can choose a few eigenmodes on which to focus, ignoring

the effect of the others. If the eigenvectors are ordered in descending value of  $|\lambda|$ , we can define some cutoff  $\tilde{N}$  and write the field as

$$\tilde{\boldsymbol{\phi}} = \sum_{n=0}^{\tilde{N}} c_n \mathbf{v}_n. \quad (17)$$

The upper limit of the summation,  $\tilde{N}$ , is chosen to maximize the figure of merit, defined as the overlap integral with the desired radiation pattern with  $|\tilde{\mathbf{E}}|$  in the far field. Due to interference of the modes, this is not achieved by adding all of the modes together but only a small subset of them. This process is illustrated in the Supplemental Material [44]. In this way, even a very complex scattering system can be described in terms of a few resonances. We have chosen to consider the modes with the largest eigenvalues as these represent modes that enhance the incident field the most [43], due to multiple-scattering effects. The application of this analysis to our designs is shown in Fig. 8.

Figures 8(a)–8(c) show this analysis for the one-beam device that we have designed. The location of the eigenvectors of the interaction matrix in the complex plane are given in Fig. 8(a), color coded by  $|\lambda|$ . Considering the eigenmodes with the two largest eigenvalues, the far and near fields are plotted in Figs. 8(b) and 8(c) respectively. We see from the far field that the response of the device is strongly dominated by these two modes. More interestingly, examining the field shown in Fig. 8(c) we can see how the device operates. Interpreting the operation in the language of the Yagi-Uda antenna, part of the structure acts as “directors” and some acts as a “reflector.” The directors act to create the beam in the desired direction, while the reflector blocks backward radiation.

Similar arguments can be used to understand the two-lobe device, the analysis of which is shown in Figs. 8(d)–8(f). Drawing out the key behavior of the device now requires us to include the 17 modes with the largest eigenvalues. The resulting behavior of the device is a result of the superposition of these modes. As the complexity of the desired field grows, more eigenmodes contribute to the response. Examining the field shown in Fig. 8(f), one can again see certain parts of the array acting as directors and some acting as reflectors.

Finally, we apply this analysis to our three-lobe device. To reconstruct the key behavior of this device, we include the modes with the 25 largest eigenvalues. Once again, the field shown in Fig. 8(i) exhibits clear amplitude peaks in the directions of the lobes. One can also see from the field of the modes that the lobes will differ in width. While the field clearly shows the lobes, there are other field hot spots such as those at  $(-2\lambda, 0)$  and  $(3\lambda, -2\lambda)$ . The function of these regions is important for the performance of the device but without this modal-analysis picture one would not expect these parts of the array to play an important role.

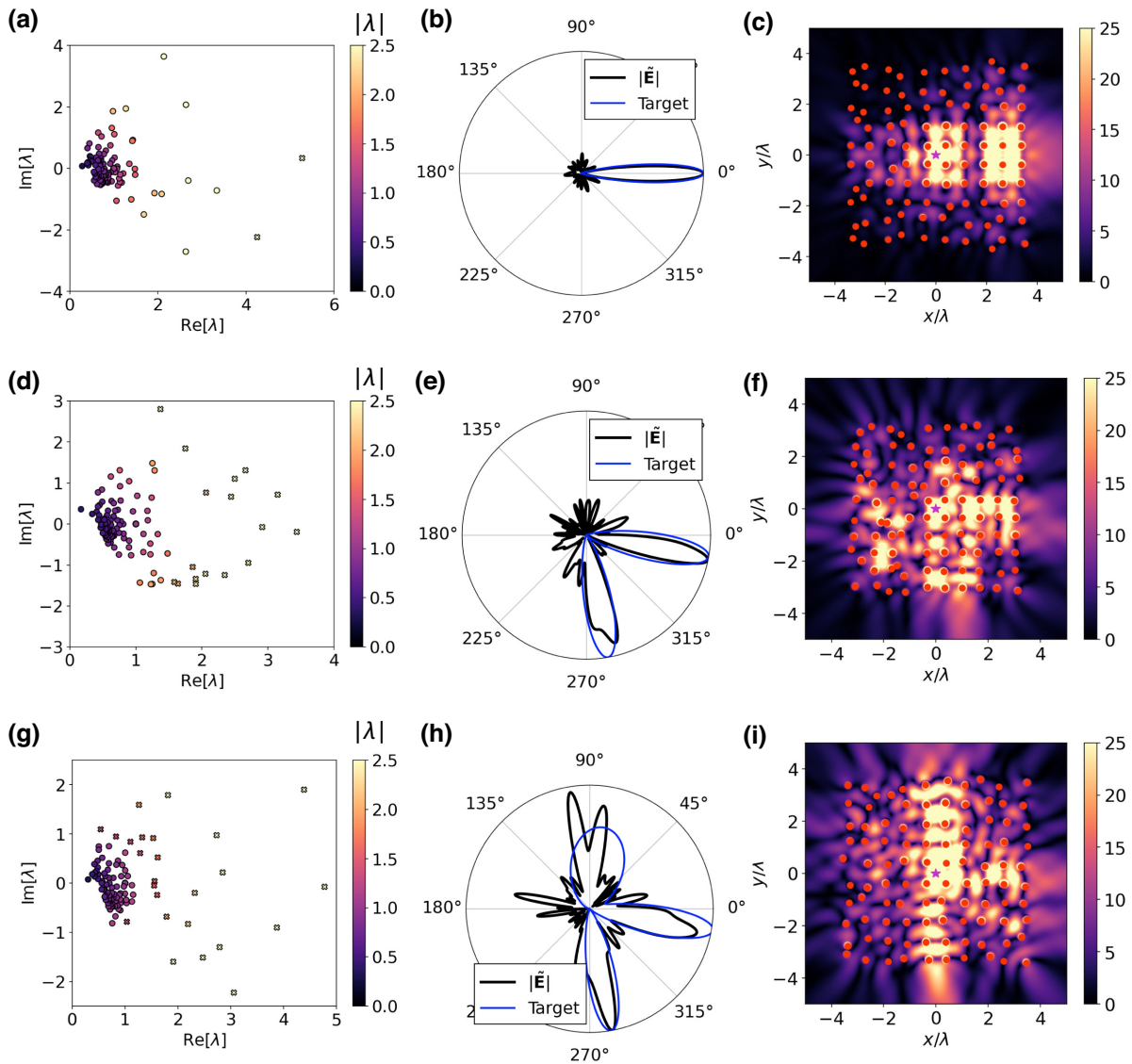


FIG. 8. The eigenmode analysis of (a)–(c) the one-lobe device, (d)–(f) the two-lobe device, and (g)–(i) the three-lobe device. Panels (a), (d), and (g) show the distribution of the eigenvalues of the interaction matrix in the complex plane, with the color scale indicating the magnitude of the eigenvalue. The response of the system is expanded into the  $\tilde{N}$  modes with the largest eigenvalues. These are indicated as crosses in (a), (d), and (g). The radiation patterns associated with this expansion are shown in (b), (e), and (h), showing the two, 17, and 25 largest eigenvalues, respectively, with the near fields ( $|\vec{E}|$ ) shown in (c), (f), and (i). While the modal fields are independent of the emitter, the location of the source in the experiments is indicated with a magenta star and the rods by red dots.

This is the key benefit of being able to apply this analysis technique. Collective behavior is key to the performance of our designs and this method allows one to investigate (i) to what extent collective behavior is important and (ii) which parts of the array are crucial to this response. Such analysis is helpful for fault tolerance as well as to provide insight into the structures.

### V. CONCLUSIONS AND OUTLOOK

We have experimentally demonstrated a new framework for manipulating the radiation from simple sources. To

meet the challenges of the next generation of communications, antenna functionality can be moved into the design of a passive material instead of the antenna itself, so that feeding remains simple but functionality can be complex. While active elements could be included in our design methodology, there are many situations in which static but nonstandard beam shapes are required. For example, many indoor applications will require beam shapes specific to the building or room shape. The ability to use a cheap and simple metamaterial layer to meet this requirement, rather than increasing the electrical complexity of the source, might be desirable for next-generation communications.

The paradigm that we have presented here is both simple and versatile. Passive scattering elements and the emitter are characterized by full-wave simulations independently and then the coupled-dipole approximation is used to model the whole system. While this approach introduces some numerical errors, it enables the modeling of otherwise numerically inaccessible systems. Inverse design of the scattering systems has then been performed using gradient descent, with gradients that can be efficiently evaluated, as we have derived their analytical form. Several experimental results are presented that illustrate both the utility and limitations of our method.

Future work might focus on the design of switchable or time-varying structures, so that the antenna functionality can be tuned in real time. While our results have focused on a single polarization, more exotic polarization manipulation could be achieved with bianisotropic or chiral passive scatterers. Broadening the bandwidth by including multiple species of scatterers supporting resonances at different spectral locations, or of different multipolar nature, would also be of great utility in the context of antennas.

All data and code created during this research are openly available from the corresponding authors, upon reasonable request.

### ACKNOWLEDGMENTS

J.R.C. would like to thank D. A. Patient and I. R. Hooper for many useful discussions. We acknowledge financial support from the Engineering and Physical Sciences Research Council (EPSRC) of the United Kingdom, via the EPSRC Centre for Doctoral Training in Metamaterials (Grant No. EP/L015331/1). J.R.C. also wishes to acknowledge financial support from the Defence Science Technology Laboratory (DSTL). L.D.S. wishes to acknowledge financial support from Leonardo Ltd UK via the Industrial Cooperate Award in Science and Technology studentship grant (Grant No. EP/R511924/1). A.W.P. acknowledges financial support from the Royal Academy of Engineering under the Research Fellowship scheme. S.A.R.H. acknowledges financial support from the Royal Society (Grant No. URF\R\211033).

- 
- [1] U. Leonhardt and T. G. Philbin, General relativity in electrical engineering, *New J. Phys.* **8**, 247 (2006).
  - [2] J. B. Pendry, D. Schurig, and D. R. Smith, Controlling electromagnetic fields, *Science* **312**, 5781 (2006).
  - [3] N. Kaina, F. Lemoult, M. Fink, and G. Lerosey, Negative refractive index and acoustic superlens from multiple scattering in single negative metamaterials, *Nature* **525**, 77 (2015).
  - [4] M. Kadic, G. W. Milton, M. van Hecke, and M. Wegener, 3D metamaterials, *Nat. Rev. Phys.* **1**, 198 (2019).

- [5] Y. Hua, C. Qian, H. Chen, and H. Wang, Experimental topology-optimized cloak for water waves, *Mater. Today Phys.* **27**, 100754 (2022).
- [6] L. Shen, B. Zheng, Z. Liu, Z. Wang, S. Lin, S. Dehdashti, E. Li, and H. Chen, Large-scale far-infrared invisibility cloak hiding object from thermal detection, *Adv. Opt. Mater.* **3**, 1738 (2015).
- [7] B. A. Munk, *Frequency Selective Surfaces: Theory and Design* (John Wiley and Sons, New York, 2000).
- [8] J. D. Joannopoulos, S. G. Johnson, J. N. Winn, and R. D. Meade, *Photonic Crystals: Molding the Flow of Light* (Princeton University Press, Princeton and Oxford, 2008).
- [9] H. Cao, A. P. Mosk, and S. Rotter, Shaping the propagation of light in complex media, *Nat. Phys.* **18**, 994 (2022).
- [10] M. Horodyski, M. Kühmayer, C. Ferise, S. Rotter, and M. Davy, Anti-reflection structure for perfect transmission through complex media, *Nature* **607**, 281 (2022).
- [11] P. del Hougne, R. Sobry, O. Legrand, F. Mortessagne, U. Kuhl, and M. Davy, Experimental realization of optimal energy storage in resonators embedded in scattering media, *Laser Photonics Rev.* **15**, 2000335 (2021).
- [12] K. Pichler, M. Kühmayer, J. Böhm, A. Brandstötter, P. Ambichl, U. Kuhl, and S. Rotter, Random anti-lasing through coherent perfect absorption in a disordered medium, *Nature* **576**, 351 (2019).
- [13] J. Sol, D. R. Smith, and P. del Hougne, Meta-programmable analog differentiator, *Nat. Commun.* **13**, 1713 (2022).
- [14] A. P. Mosk, A. Lagendijk, G. Lerosey, and M. Fink, Controlling waves in space and time for imaging and focusing in complex media, *Nat. Photonics* **6**, 283 (2012).
- [15] Y. Brûlé, P. Wiecha, A. Cuche, V. Paillard, and G. C. des Francs, Magnetic and electric Purcell factor control through geometry optimization of high index dielectric nanostructures, *Opt. Express* **30**, 20360 (2022).
- [16] P. R. Wiecha, A. Arbouet, C. Girard, A. Lecestre, G. Larrivé, and V. Paillard, in *Proc. SPIE 10694, Computational Optics II* (Frankfurt, Germany, 2018), p. 1069402.
- [17] P. R. Wiecha, C. Majorel, C. Girard, A. Cuche, V. Paillard, O. L. Muskens, and A. Arbouet, Design of plasmonic directional antennas via evolutionary optimization, *Opt. Express* **27**, 29069 (2019).
- [18] I. F. Akyildiz, A. Kak, and S. Nie, 6G and beyond: The future of wireless communications systems, *IEEE Access* **8**, 133995 (2020).
- [19] S. Mignuzzi, S. Vezzoli, S. A. R. Horsley, W. L. Barnes, S. A. Maier, and R. Sapienza, Nanoscale design of the local density of optical states, *Nano Lett.* **19**, 1613 (2019).
- [20] L. D. Stanfield, A. W. Powell, S. A. R. Horsley, J. R. Sambles, and A. P. Hibbins, Microwave demonstration of Purcell effect enhanced radiation efficiency, *Sci. Rep.* **13**, 5065 (2023).
- [21] Robert Bennett and S. Y. Buhmann, Inverse design of light-matter interactions in macroscopic QED, *New J. Phys.* **22**, 093014 (2020).
- [22] R. Bennett, Inverse design of environment-induced coherence, *Phys. Rev. A* **103**, 013706 (2021).
- [23] J. Matuszak, S. Y. Buhmann, and R. Bennett, Shape optimizations for body-assisted light-matter interactions, *Phys. Rev. A* **106**, 013515 (2022).

- [24] S. Molesky, Z. Lin, A. Y. Piggott, W. Jin, J. Vucković, and A. W. Rodriguez, Inverse design in nanophotonics, *Nat. Photonics* **12**, 659 (2018).
- [25] Q. Tan, C. Qian, T. Cai, B. Zheng, and H. Chen, Solving multivariable equations with tandem metamaterial kernels, *Prog. Electromagn. Res.* **175**, 139 (2022).
- [26] P. R. Wiecha, A. Arbouet, C. Girard, and O. L. Muskens, Deep learning in nano-photonics: Inverse design and beyond, *Photonics Res.* **9**, B182 (2021).
- [27] Y. Shou, Y. Feng, Y. Zhang, H. Chen, and H. Qian, Deep learning approach based optical edge detection using ENZ layers, *Prog. Electromagn. Res.* **175**, 81 (2022).
- [28] G. G. Roy, S. Das, P. Chakraborty, and P. N. Suganthan, Design of non-uniform circular antenna arrays using a modified invasive weed optimization algorithm, *IEEE Trans. Antennas Propag.* **59**, 110 (2010).
- [29] K. Grotov, D. Vovchuk, S. Kosulnikov, I. Gorbenko, L. Shaposhnikov, K. Ladutenko, P. Belov, and P. Ginzburg, Genetically designed wire bundle superscatterers, *IEEE Trans. Antennas Propag.* **70**, 9621 (2022).
- [30] D. Silverstein and Y. Leviatan, Design of irregular embedded antenna arrays for shaped-beam radiation using reciprocity and sparse optimization, *IEEE Trans. Antennas Propag.* **71**, 3273 (2023).
- [31] S. E. Nai, W. Ser, Z. L. Yu, and H. Chen, Beam pattern synthesis for linear and planar arrays with antenna selection by convex optimization, *IEEE Trans. Antennas Propag.* **58**, 3923 (2010).
- [32] F. Yang, S. Yang, Y. Chen, S. Qu, and J. Hu, Synthesis of sparse antenna arrays subject to constraint on directivity via iterative convex optimization, *IEEE Antennas Wirel. Propag. Lett.* **20**, 1498 (2021).
- [33] R. Harrington, Reactively controlled directive arrays, *IEEE Trans. Antennas Propag.* **26**, 390 (1978).
- [34] J. D. Kraus and R. J. Marhefka, *Antennas for all Applications* (McGraw Hill, New York, 2003).
- [35] M. Di Renzo, M. Debbah, D.-T. Phan-Huy, A. Zappone, M.-S. Alouini, C. Yuen, V. Sciancalepore, G. C. Alexandropoulos, J. Hoydis, H. Gacanin, J. de Rosny, A. Bounceur, G. Lerosey, and M. Fink, Smart radio environments empowered by reconfigurable ai meta-surfaces: An idea whose time has come, *Eurasip J. Wirel. Commun. Netw.* **129**, 2019 (2019).
- [36] T. Hirsch, M. Liertzer, D. Pogany, F. Mintert, and S. Rotter, Pump-controlled directional light emission from random lasers, *Phys. Rev. Lett.* **111**, 023902 (2013).
- [37] L. L. Foldy, The multiple scattering of waves. I. General theory of isotropic scattering by randomly distributed scatterers, *Phys. Rev.* **67**, 107 (1945).
- [38] E. M. Purcell and C. R. Pennypacker, Scattering and absorption of light by nonspherical dielectric grains, *Astrophys. J.* **186**, 705 (1973).
- [39] A. B. Evlyukhin, C. Reinhardt, and B. N. Chichkov, Multipole light scattering by nonspherical nanoparticles in the discrete dipole approximation, *Phys. Rev. B* **84**, 235429 (2011).
- [40] A. B. Evlyukhin, C. Reinhard, E. Evlyukhin, and B. N. Chichkov, Multipole analysis of light scattering by arbitrary-shaped nanoparticles on a plane surface, *J. Opt. Soc. Am. B* **30**, 2589 (2013).
- [41] J. R. Capers, S. J. Boyes, A. P. Hibbins, and S. A. R. Horsley, Designing disordered multi-functional metamaterials using the discrete dipole approximation, *New J. Phys.* **24**, 113035 (2022).
- [42] H. Levine and J. Schwinger, On the theory of electromagnetic wave diffraction by an aperture in an infinite plane conducting screen, *Commun. Pure Appl. Math.* **3**, 355 (1950).
- [43] J. R. Capers, S. J. Boyes, A. P. Hibbins, and S. A. R. Horsley, Designing the collective non-local responses of metasurfaces, *Commun. Phys.* **4**, 209 (2021).
- [44] See the Supplemental Material at <http://link.aps.org/supplemental/10.1103/PhysRevApplied.21.014005> for details of how the figure of merit is expanded to find the gradient; a detailed experimental and numerical characterization of the monopole source; a photograph of the experimental setup; an analysis of possible sources of experimental errors;  $s_{11}$  measurements of the devices; an investigation of how changing the number of scatterers changes the results of the optimization; and a discussion of how the eigenmodes interfere with each other when they are added. The Supplemental Material also contains Ref. [52].
- [45] M. Yazdi and N. Komjani, Polarizability tensor calculation using induced charge and current distributions, *Prog. Electromagn. Res. M* **45**, 123 (2016).
- [46] M. Yazdi and N. Komjani, Polarizability calculation of arbitrary individual scatterers, scatterers in arrays, and substrated scatterers, *J. Opt. Soc. Am. B* **33**, 491 (2016).
- [47] P. A. Belov, S. I. Maslovski, K. R. Simovski, and S. A. Tretyakov, A condition imposed on the electromagnetic polarizability of a bianisotropic lossless scatterer, *Tech. Phys. Lett.* **29**, 718 (2003).
- [48] COMSOL MULTIPHYSICS v. 6.1. [www.comsol.com](http://www.comsol.com). Comsol ab, Stockholm, Sweden.
- [49] A. E. Olk, P. E. M. Macchi, and D. A. Powell, High-efficiency refracting millimeter-wave metasurfaces, *IEEE Trans. Antennas Propag.* **68**, 5453 (2020).
- [50] Z. Wang, B.-Z. Wang, J.-P. Liu, and R. Wang, Method to obtain the initial value for the inverse design in nanophotonics based on a time-reversal technique, *Opt. Lett.* **46**, 2815 (2021).
- [51] P. A. Martin, *Multiple Scattering: Interaction of Time-Harmonic Waves with N Obstacles* (Cambridge University Press, Cambridge, 2006).
- [52] L. J. Chu, Physical limitations of omni-directional antennas, *J. Appl. Phys.* **19**, 1163 (1948).